Comparative Analysis of XANES and EXAFS for Local Structural Characterization of Disordered Metal Oxides

Junying Li[a], Yuanyuan Li[a], Prahlad K. Routh[a], Evgeniy Makagon[b], Igor Lubomirsky[b] and Anatoly I. Frenkel[a]*

[a]Department of Materials Science and Engineering, Stony Brook University, Stony Brook, New York, 11794, USA
[b]Department of Materials and Interfaces, Weizmann Institute of Science, Rehovot, 7610001, Israel

*Correspondence email: Anatoly.Frenkel@stonybrook.edu

Synopsis This article evaluates the utility of pre-edge analysis of X-ray absorption near edge structure spectra for studying materials with variable amount of disorder using two examples: 1) a unimodal distribution of nearest neighbors of homogeneously distributed metal centers (Ti in Ti oxide nanocomposites) and 2) a bimodal distribution due to the local structural heterogeneities around V in V oxide nanocomposites. In the latter case, both the pre-edge analysis and conventional EXAFS analysis are combined to detect the presence of local structural heterogeneities.

Abstract In functional materials, the local environment around active species that may contain just a few nearest neighboring atomic shells often change in response to the external conditions. Strong disorder in the local environment poses a challenge to commonly used extended X-ray absorption fine structure (EXAFS) analysis. Furthermore, the dilute concentrations of absorbing atoms, small sample size, and the constraints of the experimental setup often limit the utility of EXAFS for structural analysis. X-ray absorption near edge structure (XANES) has been established as a good alternative method to provide local electronic and geometric information of materials. The pre-edge region in the XANES spectra of metal compounds is a useful but relatively under-utilized resource of information about the chemical composition and structural disorder in nano-materials. In this study, we demonstrate two examples of materials in which the transition metal environment is either relatively symmetric or strongly asymmetric. In the former case, EXAFS results agree with those obtained from the pre-edge XANES analysis, while, in the latter case, they are in a seeming contradiction. We reconcile the two observations by revisiting the limitations of EXAFS in the case of a strong, asymmetric bond length disorder, expected for mixed-valence oxides, and emphasize

the utility of the pre-edge XANES analysis for detecting local heterogeneities in structural and compositional motifs.

Keywords: Functional materials, XAFS, pre-edge analysis, local symmetry

1. **Introduction**

In functional materials, the local environment around various atomic species may change dynamically under different operando conditions, such as elevated temperature, pressure, and application of external electric fields (Vaccari *et al.*, 2009; Dalba *et al.*, 2004)). The local atomic displacements introduce distortions in the bond lengths, as a result affecting specific functional properties, such as piezoelectricity, ferroelectricity, and pyroelectricity (Abrahams *et al.*, 1978). A variety of experimental methods such as atomic-scale microscopy, X-ray diffraction (XRD), and X-ray photoelectron spectroscopy (XPS) are developed and utilized to study these changes (Ueda, 2013; Feldmann, 2003 & Wang *et al.*, 2013). Nevertheless, the choice of tools for detecting and interpreting small structural changes in functional materials is limited. X-ray absorption spectroscopy (XAS) is a premier technique to probe the structure at the atomic scale (Rehr et al.,2000; Sayers *et al.*,1971; Bingham *et al.*,2014; Wende, 2004; Penner-Hahn, 1999; Grunes, 1983; Farges *et al.*, 2004; Sayers *et al.*,1969; Ankudinov *et al.*, 2002; & Frenkel *et al.*, 2001). In particular, extended X-ray absorption fine structure (EXAFS) provides essential information on the distribution of neighboring atoms around the absorbing atom, which has excellent sensitivity to local atomic displacement and is element-specific. EXAFS analysis commonly assumes Gaussian distribution of bond lengths, which is usually sufficient to understand the local symmetry of well-defined materials, such as homogeneous, single-phase bulk solids (Timoshenko *et al.*, 2019). However, interatomic distance distribution can be more complicated in many materials, such as metallic nanoparticles, mesoporous materials, and metals in molten salts (Boubnov *et al.*, 2020; Prasai *et al.*, 2015; Billinge & Levin, 2007; McGreevy & Pusztai, 1990; Dias *et al*., 2021), where the local atomic environment is characterized by strong asymmetry in the bond length distribution. Such an asymmetry has been shown to be a source of artifacts in conventional structural analysis methods by EXAFS (Yevick & Frenkel, 2010). In these cases, the non-Gaussian distribution of bond length needs to be accounted for in order to understand the local environment, which introduces the inaccuracy of quantitative analysis of experimental EXAFS spectra. The alternative approaches used to circumvent the limitations of conventional EXAFS analysis are generating the theoretical EXAFS spectra based on atomic-level simulations, e.g., molecular dynamics (MD) or reverse Monte Carlo simulations (RMC) methods (Chill *et al.*, 2015; Yancey *et al.*, 2013 & Gurman *et al.*, 1990). The accuracy of the theoretical EXAFS spectra can be confirmed by the experimental EXAFS spectra and

then determining the atomic structures. In the MD simulation method, the interatomic forces are derived from ab initio calculation or empirical force fields (Chill *et al.*, 2015; Cicco *et al.*, 2002 & Roscioni *et al.*, 2011). Although this approach can be employed to study the local structure by modeling thermal disorder and anharmonic effects, the MD simulation method is limited to simulations of the smaller clusters (1~2 nm in size) (Mazzone *et al.*, 2008). In RMC, the configuration-averaged EXAFS is calculated after the positions of the atoms in the assumed 3D structure model are randomly modified at each interaction, and then, the optimized structure is generated after minimizing the difference with the experimental and calculated EXAFS (McGreevy *et al.*, 1988)

X-ray absorption near edge structure (XANES) can be employed as a complementary method to EXAFS to obtain local electronic and geometric information because it is sensitive to the electronic transitions and the multiple-scattering contributions from neighboring atoms (Rehr *et al.*, 1992 & Ankudinov *et al.*, 2002). Furthermore, the pre-edge features in the XANES spectra also contain information about the electronic and structural properties of materials (Srivastava *et al.*, 1973). The pre-edge features and the main-edge features of the experimental XANES spectra of some transition metals are well studied through understanding the features in theoretical XANES spectra, which are typically obtained by the so-called forward modeling approach (Rehr et al., 2000; Joly, 2001 &Vinson, 2011). For example, Farges *et al.* (Farges *et al.*, 1997). have successfully modeled the Ti K-edge XANES spectra for selected Ti compounds using the ab initio real space multi-scattering approach (FEFF) to interpret the features of the experimental XANES spectra, including the pre-edge features and main-edge features, providing a quantitative description of the Ti K-edge XANES spectra. Farges *et al*. show that the shapes of the XANES spectra are affected by the size and the types of clusters around the Ti atoms. In addition to that, the characteristic pre-edge features associated with the coordination number of a central atom have been utilized as a powerful tool to help understand the local symmetry (Farges *et al.*, 1997). As explained by Farges et al., for the Ti^{4+} species, the pre-edge energy position and pre-edge intensity are well separated for the different coordination numbers. Other works discussed the pre-edge features according to the group theory calculations and indicated that, although the oxidation states can be the same, the different types of symmetries, e.g. tetrahedral (T_d) and octahedral (O_h) ones, affect the intensities of the pre-edge features differently (Yamamoto, 2008). More recent applications of the sensitivity of the pre-edge features to the local environment of metal oxides were used as a basis of the machine network-based approaches to predict the XANES spectra of metal oxides with quantitative accuracy (Liu *et al*., 2020, Carbone *et al.*, 2020 & Torrisi *et al*, 2020).

In general, the results obtained by XANES such as charge states and local geometry are used to support the information extracted by EXAFS analysis, such as coordination numbers. However, as for the materials

with strong asymmetry in the bond length distribution, the results obtained by XANES and EXAFS could be inconsistent. In addition to that, in functional materials, dilute concentrations of absorbing atoms, low dimensionality of sample size, and the experimental setup, e.g., reaction cell walls, pose obstacles toward collecting the experimental EXAFS spectrum with sufficient quality for adequate structural analysis. In these cases when the EXAFS analysis is unavailable or unreliable, the pre-edge analysis stands out as the sole source of information on the local symmetry from X—ray absorption measurement.

In this study, we illustrate this problem – the inconsistency in the determination of the local environment by XANES and EXAFS when strongly asymmetric disorder in the bonding distribution is present – using an example of two different metal oxide nanocomposite materials, in which the transition metal's local environment is either distorted octahedral, i.e., relatively symmetric, or strongly asymmetric. In the former case, EXAFS results agree with those obtained from the pre-edge analysis. In the latter case, they are inconsistent because conventional EXAFS is affected by the strong and asymmetric disorder. We focus on the Ti-doped $Ce_{0.8}Gd_{0.2}O_{1.9}$ (TiGDC20) and V-doped $Ce_{0.8}Gd_{0.2}O_{1.9}$ (VGDC20) nanocomposites, which are shown to have different local symmetries for transitional metals environment (*vide infra*). In the case of the Ti environment, although there is a high disorder, the environment is distorted octahedral. We demonstrate that, in this case, the EXAFS results and pre-edge analysis results are consistent. TiGDC20 composites were recently shown to have exceptionally high oxygen diffusion coefficient at room temperature ($\approx 10^{-14}\ cm^2/s$) and reversible oxidation-reduction cycling. This unique property led to the demonstration of an electro-chemo-mechanical (ECM) actuator working at room temperature (Makagon *et al.*, 2020). Thus understanding the local structure of such composites may have direct and immediate implication for advancement of ECM materials and applications. For the V environment, conventional EXAFS analysis shows an underestimation of coordination numbers. The possible explanations for the apparent inconsistency are that they have a heterogeneous environment with a multimodal distribution of bonds or a unimodal but strongly asymmetric environment. To investigate these effects, we performed a more in-depth pre-edge analysis to study the local symmetry of the above materials, as discussed in the rest of the article.

2. **Experimental details**

Nanocomposite thin films were fabricated according to the previously published method (Makagon *et al.*, 2020). Namely, TiGDC20 (GDC20: 20% Gd doped ceria) composites were deposited by a magnetron co-sputtering method on SiO_2 substrates with a 100 nm Al adhesion layer. Sample 1 was deposited from a Ti 2" metallic target and a GDC20 3" stoichiometric oxide target (Ar flow: 30 sccm, deposition pressure: 20 mTorr, DC power on Ti: 150Watt, RF power on GDC20: 100Watt, deposition time: 4h, estimated

thickness:1μm). In Sample 2, the oxide target was replaced with a GDC20 alloy (Ar flow: 35 sccm, O_2 flow: 3 sccm, deposition pressure: 15 mTorr, DC power on Ti: 150 Watt, RF power on GDC20: 100 Watt, deposition time: 3h, estimated thickness: 0.5μm). VGDC20 samples were deposited under the similar conditions as Sample 1 (DC power on V 2" metallic target: 100 Watt, RF power on GDC20: 100 Watt, deposition time: 4h, estimated thickness: 200-500 nm). All samples were annealed in vacuum at 430°C for 4h. Ti oxidation states and the overall grain morphology is expected to vary significantly between the samples. Ti (4966 eV) and V (5465 eV) K-edge X-ray absorption spectra of the TiGDC20 and VGDC20 thin films were measured at the QAS (7-BM) Beamline, National Synchrotron Light Source II (NSLS-II) at Brookhaven National Laboratory. X-ray absorption spectra were collected in fluorescence mode at grazing incidence. The experimental setup is shown in Figure S1. The raw XAFS data were analyzed utilizing the Athena and Artemis interfaces of the Demeter software package (Ravel & Newville, 2005). The spectra were energy-aligned, merged, and normalized.

3. Results and discussion

3.1. The local structure of Ti in nanocomposites

For the Ti K-edge XANES spectra of Sample 1 and Sample 2, as shown in Figure 1, the rising edge positions resemble that of amorphous $BaTiO_3$ (Frenkel *et al.*, 2005), suggesting that the oxidation state of Ti in Sample 1 and Sample 2 is close to Ti^{4+}. As shown in Figure S2, the oxidation state of Ti in Sample 1 is slightly lower than that in Sample 2. The inset in Figure 1 shows the pre-edge feature A corresponding to the 1s to 3d transition in Ti. As demonstrated earlier (Farges *et al.*, 1997 & Frenkel *et al.*, 2005), the intensities and energy positions of pre-edge peaks for Ti^{4+} species are well separated for different types of Ti local environment (see Figure 2). The energy position of Sample 1 and Sample 2 are aligned to compare with the components in the references (Farges *et al.*, 1997 & Frenkel *et al.*, 2005), which allows us to conclude that local environments of Ti in Sample 1 and Sample 2 are octahedral.

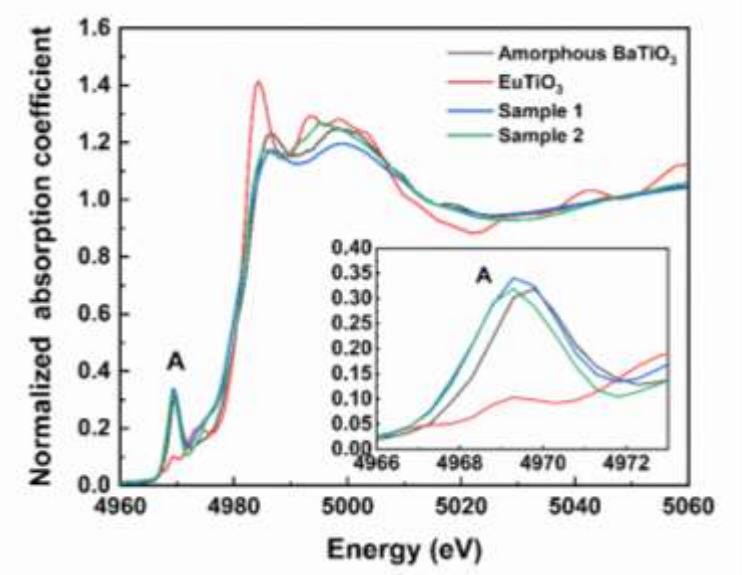

Figure 1 Ti K-edge XANES spectra of Sample 1, Sample 2, $EuTiO_3$, and amorphous $BaTiO_3$. The inset shows the zoomed-in pre-edge features (Peak A).

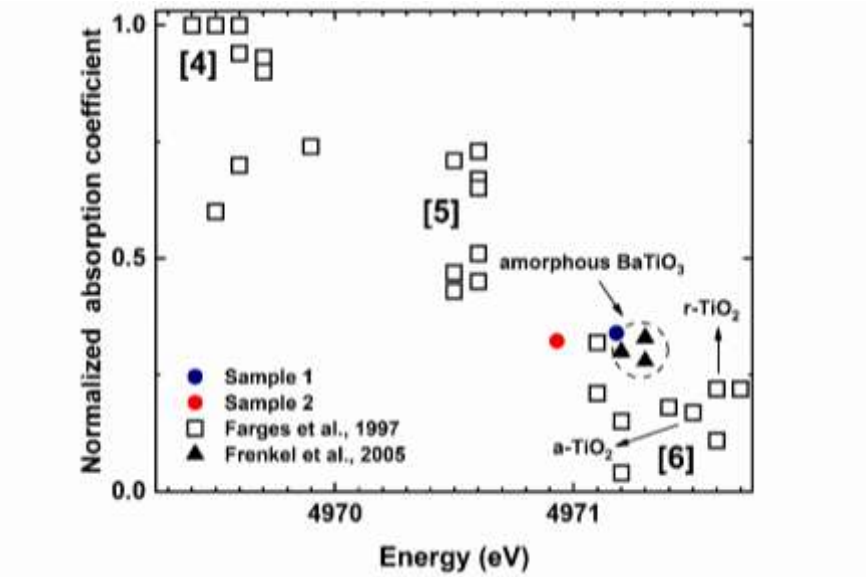

Figure 2 Normalized pre-edge height vs. energy position for Ti K-pre-edge features in the model compound. There are three domains for fourfold, fivefold, and sixfold coordinated Ti. Open squares (reproduced with permission) are from references (Farges *et al.*, 1997 & Frenkel *et al.*, 2005). Black triangles refer to the amorphous $BaTiO_3$ from (Frenkel *et al.*, 2005). Color symbols refer to the values obtained by the experimental XANES spectra in this work.

EXAFS analysis provides quantitative local structural information around Ti atoms. The coordination numbers (CN) for the Ti-O bonds obtained by EXAFS fitting of Sample 1 and Sample 2 are 5.5±1.0 and 6.1±1.0, respectively, as shown in Table 1. Hence, the local environment of Ti estimated by EXAFS analysis and taking into account the error bars is consistent with that of TiO_6 as also inferred from the XANES pre-edge features. The experimental EXAFS data and theoretical fits of Sample 1 and Sample 2 are shown in Figure 3 in r-space. EXAFS analysis indicates also that that Samples 1 and 2 differ with respect to the next nearest neighbor (Ti-Ti) distribution. As shown in Figure 3, EXAFS data for Sample 1 has a prominent second peak that corresponds to the Ti-Ti photoelectron path, which is not observed in Sample 2.

Table 1 The bond lengths (R) and disorder parameters (σ^2) of the two samples. The σ^2 value for Ti-Ti and Ti-O contributions was constrained to be the same in the fit, to lower the uncertainties.

Sample 1	Path	CN	R (Å)	σ^2 (Å^2)
#1	Ti-O	5.5±1.0	1.91±0.02	0.008±0.003
	Ti-Ti	1.6±0.8	3.01±0.09	0.008
#2	Ti-O	6.1±1.0	1.91±0.02	0.005±0.003

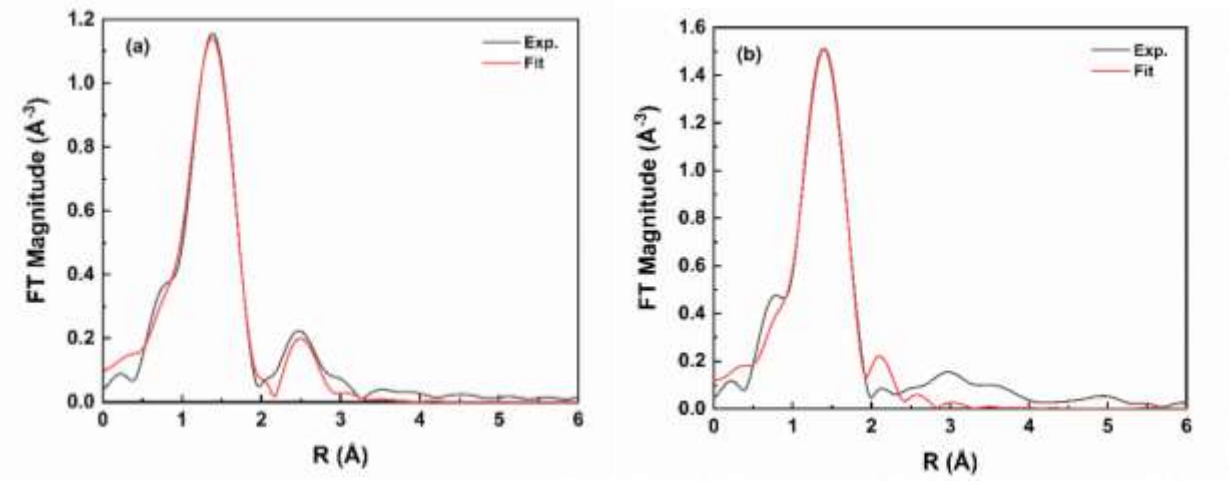

Figure 3 Fourier transform magnitudes of k^2-weighted EXAFS spectra of (a) Sample 1 and (b) Sample 2 and their theoretical fits. The k- range used in Fourier transforms was from 2 to 9 Å^{-1}. The r- range used for fitting the data for Samples 1 and 2 was 1-3.27 Å and 1-2 Å, respectively.

In addition to the coordination number and bond length, EXAFS analysis also provides information on the disorder in the TiO_6 octahedron. A related information which can be obtained by a more in-depth pre-edge analysis is on the off-center displacement d_i of the Ti atom from the center of the TiO_6 octahedron. We now discuss the relationship between the off-center displacement of the Ti atom to the disorder (σ^2) obtained by the EXAFS analysis in Sample 1 and Sample 2. The pre-edge area provides quantitative information on the off-center displacement. The area A_i of this pre-edge feature is proportional to the square of the off-center displacement (Ravel *et al.*, 1998; Ravel, 1995), as shown in Equation (1).

$$A_i = \frac{\gamma_i}{3} d_i^2. \tag{1}$$

At 300 K, the experimentally measured constants: γ_{BaTiO_3} and γ_{EuTiO_3} are 11.2 eV/Å^2 and 13.6 eV/Å^2, respectively. We assume the value of γ_{TiO_x} to be as the average of γ_{BaTiO_3} and γ_{EuTiO_3}: 12.4 eV/Å^2. $EuTiO_3$ is a centrosymmetric perovskite. The off-center displacement of $EuTiO_3$ is 0.103 Å at 300 K (Ravel *et al.*, 1998; Ravel, 1995), which refers to vibrational disorder within the TiO_6 octahedra. When calculating the off-center displacement of our samples, the peak area of $EuTiO_3$ is subtracted to correct for the thermal motion, as shown in Equation (2).

$$A_{TiO_x} - A_{EuTiO_3} = \frac{\gamma_{TiO_x}}{3} d_{TiO_x}^2 - \frac{\gamma_{EuTiO_3}}{3} d_{EuTiO_3}^2. \tag{2}$$

The off-center displacement of Ti obtained for Sample 1 and Sample 2 are 0.455 Å and 0.433 Å, respectively, as shown in Table 2. According to the XANES and EXAFS analyses, the Ti has a 6-coordinated octahedral structure. Hence, the displacement change reflects that the Ti position changes from the octahedral center without any change in the overall local symmetry. Furthermore, the magnitude and direction of the off-center displacements of Ti atoms are the sources of the changes of individual Ti-O bond lengths (r), and must be related to the mean square relative displacement (σ^2), as shown in Equation (3):

$$\sigma^2 = \langle (r - \bar{r})^2 \rangle. \tag{3}$$

We note however that a direct comparison of the displacements estimated by EXAFS from Eq. (3) and pre-edge analysis (Eq. (1)) is very complicated. In order to compare the two values, it is essential to take into account the correlation between the displacement of Ti and O atomic positions. Such analysis can be done, e.g., by molecular dynamics simulations or multi-technique Reverse Monte Carlo refinements (Noordhoek *et al.*, 2013).

In the above analysis, the Ti samples have relatively ordered environment around Ti atoms, due to the overall octahedral symmetry. In these cases, the results obtained by EXAFS analysis and pre-edge XANES analysis are consistent with each other. The above analysis also suggests that Ti with somewhat different oxidation state shares similar local coordination, which may be a hint to the ability of these composites to undergo rapid oxidation and reduction in the ECM effect (Makagon *et al*. 2020).

Table 2 Ti atom off-center displacements obtained from ex-situ experimental XANES spectra.

	Peak area	Off-center displacement (Å)
Reference: $EuTiO_3$	0.116	0.103
Sample 1	0.924	0.455
Sample 2	0.843	0.433

3.2. The local structure of V in nanocomposites

We also employed V K-edge XANES and EXAFS data collected on the VGDC20 sample to obtain the valence states and coordination numbers. As shown in Figure 4, the rising edge position is between V_2O_4 and V_2O_5, indicating the average oxidation state of V in the sample is between V^{4+} and V^{5+}. The typical symmetry of tetravalent V can be square pyramidal (P_y) or octahedral (O_h). Pentavalent V may be present in several symmetries, such as T_d, O_h, and P_y. Therefore, for the VGDC20 sample, the average coordination number of V is expected to be higher than 4 (the exact number should depend on the mixing fraction of multiple states with different symmetries). However, the coordination number obtained by EXAFS analysis is much smaller: 2.0±0.7 (Table 3). The experimental spectra and theoretical fits in r-space are shown in Figure 5.

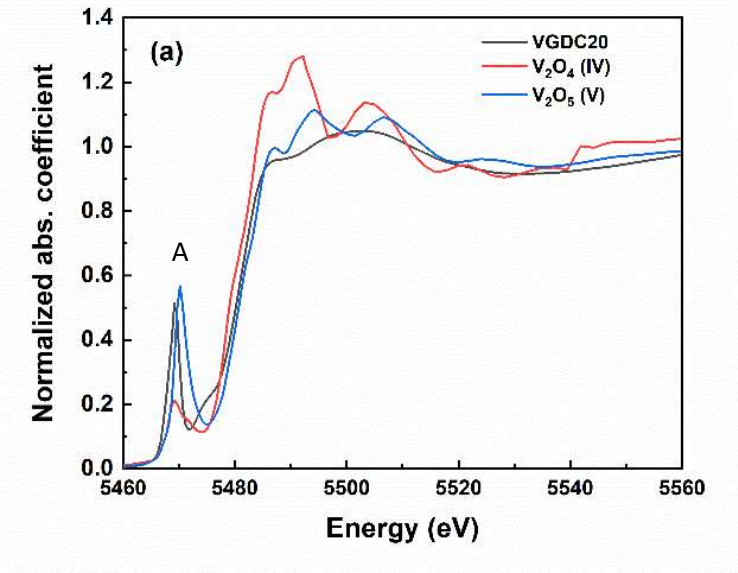

Figure 4 Normalized V K-edge XANES spectrum of VGDC20, as well as V_2O_4 and V_2O_5 standards.

To resolve the apparent discrepancy between EXAFS and XANES results for V compounds, we compare between the two possible explanations: 1) V environment is heterogeneous, containing a mixture of local structures and oxidation states, and hence, resulting in a multimodal distribution of V-O bond distances; or 2) V has the unimodal distribution of bonds but strongly asymmetric environment. To discriminate between the two possibilities, we rely on the pre-edge analysis. Giuli *et al.* followed the procedure described in (Farges *et al.*, 1997), but found that intensity and energy position of pre-edge peaks for tetravalent and pentavalent V could not be well separated because each of them contains various symmetries (Giuli *et al.*, 2004; Levina *et al.*, 2014). Therefore, an interpretation of the pre-edge peak in terms of the distortion of V atoms from the inversion symmetry center should be made with extreme caution when more than one state of V can be present in the sample. If ignored, such heterogeneity will result in an erroneous assumption that there is an "effective" V atom environment that such a method would characterize. Thus, the prevailing strategy is to use the pre-edge peak position and area for the task of speciation of structures and oxidation states of V in the sample. Only when a pure state is established, its analysis, based on the pre-edge peak intensity (Eq. 1) can be undertaken, similar to what was done above with Ti compounds.

Table 3 EXAFS analysis results for VGDC20 sample.

Sample	Path	CN	R (Å)	σ^2 (Å^2)

VGDC20	V-O bond	2.0±0.7	1.77±0.03	0.004±0.006

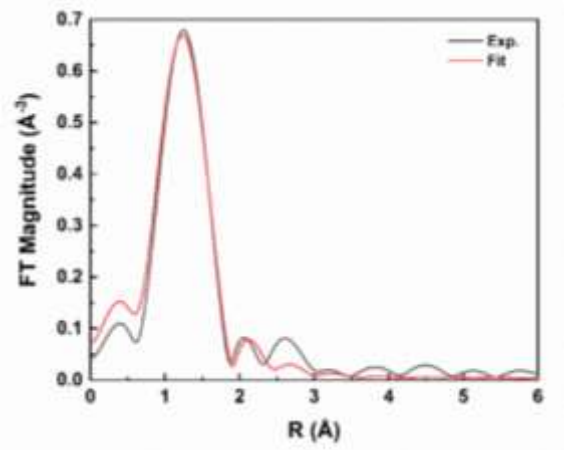

Figure 5 Experimental EXAFS data and theoretical fit for VGDC20. The EXAFS spectra were extracted in k-space, and Fourier transformation was carried out in the k- range of 2-7.5 Å^{-1}. The range selected for fitting in r-space is 1 - 2.3 Å.

To evaluate the oxidation states and the symmetry of V oxides, we followed the procedure described by Chaurand *et al.* (Chaurand *et al.*, 2007). The evaluations of the oxidation states and the local symmetry of V are performed by using the normalized pre-edge peak area and the pre-edge peak centroid energy, as shown in Figure 6. Centroid energy is defined as the area-weighted average of the position in energy ($E-E_0$) of each component contributing to the pre-edge peak. E_0 is the maximum value of the first peak of the vanadium metal derivative spectrum, which marks the threshold or onset of photo-excitation of the 1s electron in vanadium metal (Bearden & Burr, 1967). The total pre-edge area was derived by calculating the sum of each component's integrated areas in the vanadium pre-edge peak region. To correct for the possible differences in experimental conditions, we assumed that the normalized pre-edge peak area of the V_2O_5 measured in this work is the same as the value in the reference (Chaurand *et al.*, 2007). The normalized pre-edge peak area in the VGDC20 sample is placed on the curve connecting the V^{4+}(Py) and V^{5+}(Td) states, indicating the coexistence of phases characterized by the T_d and P_y environments (Figure 6). Due to the strong difference in the coordination numbers and the symmetries between the T_d and P_y environments of V coexisting in this sample, the ensemble-average EXAFS data will be expected to have a non-symmetric distribution of nearest neighboring V-O bonds, explaining the underestimation of the V-O coordination number by conventional EXAFS analysis (Table 3).

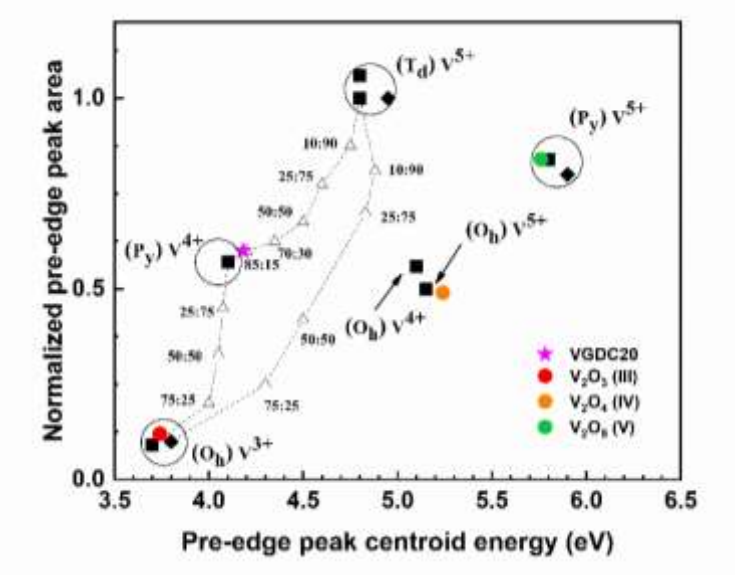

Figure 6 The plot of total pre-edge peak area (normalized according to value 1 to vanadinite) versus pre-edge peak centroid position. Black symbols, reproduced with permission, are from reference (Chaurand *et al.*, 2007) and refer to the standard compounds (■) recorded on beamline at the ESRF synchrotron and compounds (♦) recorded at Elettra synchrotron. Open triangles from reference (Chaurand *et al.*, 2007) refer to the mixtures of $(O_h)V^{3+}$ + $(Py)V^{4+}$, $(Py)V^{4+}$ + $(T_d)V^{5+}$, and $(O_h)V^{3+}$ + $(T_d)V^{5+}$. Color symbols refer to the values obtained by the experimental XANES spectra collected at QAS, NSLS-II. The color circles refer to the standards compounds: V_2O_3 (red), V_2O_4 (orange), and V_2O_5 (green), measured in this work. The pink star refers to the VGDC20 sample measured in this work.

4. Discussion and conclusions

In the functional materials, the asymmetric bond length distribution poses the challenge to obtain reliable results by the conventional EXAFS analysis. Furthermore, the low concentration of absorbing atoms, small size, and experimental setup prevent us from collecting analyzable experimental EXAFS spectra. In this paper, we demonstrated the efficacy of pre-edge XANES analysis by comparing two types of materials, with symmetric and asymmetric local structures. This capability is important for studies of a large class of materials with local disorder such as nanoscale oxides and nano-composites studied under realistic operating conditions, including recently investigated materials exhibiting electro-chemo-mechanical effects. For example, while there are no reports yet on the use of V-based nanocomposites in electro-chemo-mechanical actuation, the results shown in this work suggest that, by comparison with the Ti-based composites that feature the same locally tetrahedral environment while sustaining large bonding disorder,

strongly non-symmetric distribution in V-based composites may be non-conducive for applications that require rapid oxidation-reduction.

The analyses we presented proved useful for two cases, where the environment around all absorbing atoms is either similar (a homogeneous case, as illustrated using Ti oxide nanocomposites) or changes across the sample (a heterogeneous case, shown using V oxide nanocomposites). In the former case, supervised machine learning – assisted analysis has been demonstrated as a powerful tool for structural refinement, well beyond the relatively limited result achieved by either EXAFS analysis or pre-edge XANES fitting approach. In the latter case, a special care is needed for machine learning analysis, due to the presence of multiple inequivalent environments. For that, the deconvolution of the spectra using unsupervised approaches is required (Timoshenko, Frenkel, 2019).

Acknowledgements

We gratefully acknowledge help of Drs. Steven Ehrlich and Lu Ma with beamline experiments at the QAS beamline of NSLS-II.

Funding information

AIF, JL, YL and PKR acknowledge support by NSF Grant number DMR-1911592. IL and AIF acknowledge the NSF-BSF program grant 2018717. This research used beamline 7-BM (QAS) of the National Synchrotron Light Source II, a U.S. DOE Office of Science User Facility operated for the DOE Office of Science by Brookhaven National Laboratory under contract no. DE-SC0012704.

References

Abrahams, S. C., Laboratories, B. & Hill, M. (1978). *Mater. Res. Bull.* **13**, 1253–1258.

Ankudinov, A. L., Rehr, J. J., Low, J. J. & Bare, S. R. (2002). *J. Chem. Phys.* **116**, 1911–1919.

Bearden, J. A. & Burr, A. F.. *Rev. Mod. Phys.* **39**, 125–142.

Billinge, S. J., & Levin, I. (2007). *Science.* **316**, 561-565.

Bingham, P. A., Hannant, O. M., Reeves-McLaren, N., Stennett, M. C., & Hand, R. J. (2014). *J. Non-Cryst. Solids* **387**, 47-56.

Boubnov, A., Timoshenko, J., Wrasman, C. J., Hoffman, A. S., Cargnello, M., Frenkel, A. I. & Bare, S. R. (2020). *Radiat. Phys. Chem.* **175**, 108304.

Carbone, M. R., Topsakal, M., Lu, D. & Yoo, S. (2020). *Phys. Rev. Lett*. **124**, 156401.

Chaurand, P., Rose, J., Briois, V., Salome, M., Proux, O., Nassif, V., Olivi, L., Susini, J., Hazemann, J. L. & Bottero, J. Y. (2007). *J. Phys. Chem. B*. **111**, 5101–5110.

Chill, S. T., Anderson, R. M., Yancey, D. F., Frenkel, A. I., Crooks, R. M. & Henkelman, G. (2015). *ACS Nano*. **9**, 4036–4042.

Cicco, A. Di, Minicucci, M., Principi, E., Witkowska, A., Rybicki, J. & Laskowski, R. (2002). *J. Phys. Condens. Matter*. **14**, 3365–3382.

Dalba, G., Fornasini, P., Grisenti, R., Rocca, F. (2004). *J. Non-Cryst. Solids*, **346**, 7–15.

Dias, E. T., Gill, S. K., Liu, Y., Halstenberg, Ph., Dai, S., Huang, J., Mausz, J., Gakhar, R., Phillips, W. C., Mahuring, S., Pimblott, S. M., Wishart, J. F. & Frenkel, A. I. (2021). *J. Phys. Chem. Lett.* **12**, 157-164

Farges, F. & Brown, G. E. (1997). *Phys. Rev. B - Condens. Matter Mater. Phys.* **56**, 1809–1819.

Farges, F., Lefrère, Y., Rossano, S., Berthereau, A., Calas, G. & Brown, G. E. (2004). *J. Non. Cryst. Solids*. **344**, 176–188.

Feldmann, C. (2003). *Adv. Funct. Mater.* **13**, 101-107.

Frenkel, A. I., Feldman, Y., Lyahovitskaya, V., Wachtel, E. & Lubomirsky, I. (2005). *Phys. Rev. B -*

Frenkel, A. I., Hills, C. W., & Nuzzo, R. G. (2001). *J. Phys. Chem. B* **105**, 12689-12703.

Condens. Matter Mater. Phys. **71**, 024116.

Giuli, G., Paris, E., Mungall, J., Romano, C. & Dingwell, D. (2004). *Am. Mineral*. **89**, 1640-1646.

Grunes, L. A. (1983). *Phys. Rev. B*. **27**, 2111–2131.

Gurman, S. J., & R. L. McGreevy. (1990). *J. Phys. Condens. Matter* **2**, 9463.

Joly, Y. (2001). *Phys. Rev. B.* **63**, 125120.

Levina, A., McLeod, A. I. & Lay, P. A. (2014). *Chem. - A Eur. J.* **20**, 12056–12060.

Liu, Y., Marcella, N., Timoshenko, J., Halder, A., Yang, B., Kolipaka, L., Pellin, M., Seifert, S., Vajda, S., Liu, P. & Frenkel, A. I. (2019) *J. Chem. Phys*. **151**, 164201

Makagon, E., Wachtel, E., Houben, L., Cohen, S. R., Li, Y., Li, J., Frenkel, A. I. & Lubomirsky, I. (2020). *Adv. Funct. Mater.* **31**, 2006712.

Mazzone, G., Rivalta, I., Russo, N. & Sicilia, E. (2008). *J. Phys. Chem. C*. **112**, 6073–6081.

McGreevy, R. L., & Pusztai, L. (1988). *Mol. Simul*. **1**, 359-367.

McGreevy, R. L., & Pusztai, L. (1990). *Proc. Math. Phys. Eng. Sci.* **430**, 241-261.

Noordhoek, M. J., Krayzman, V., Chernatynskiy, A., Phillpot, S. R., & Levin, I. (2013). *Appl. Phys. Lett.* **103**, 022909.

Penner-Hahn, J. E. (1999). *Coord. Chem. Rev.* **190**–**192**, 1101–1123.

Prasai, B., Wilson, A. R., Wiley, B. J., Ren, Y., & Petkov, V. (2015). *Nanoscale*, **7**, 17902-17922.

Ravel, B., Stern, E. A., Vedrinskii, R. I., & Kraizman, V. (1998). *Ferroelectrics,* **206**, 407-430.

Ravel, Bruce, & Matthew Newville. (2005). *J. Synchrotron Radiat.* **12**, 537-541.

Ravel, B. Ph.D. thesis, University of Washington, 1995.

Rehr, J. J., Albers, R. C. & Zabinsky, S. I. (1992). *Phys. Rev. Lett.* **69**, 3397–3400.

Rehr, J. J. & Albers, R. C. (2000). *Rev. Mod. Phys.***72**, 621–654.

Roscioni, O. M., Zonias, N., Price, S. W. T., Russell, A. E., Comaschi, T. & Skylaris, C. K. (2011). *Phys. Rev. B - Condens. Matter Mater. Phys.* **83**, 115409.

Sayers, D. E., Lytle, F. W., & Stern, E. A. (1969). *Adv. X-Ray Anal.* **13**, 248-271.

Sayers, D. E., Stern, E. A., & Lytle, F. W. (1971). *Phys. Rev. Lett.* **27** 1204.

Srivastava, U. C., & Nigam, H. L. (1973). *Coord. Chem. Rev.* **9**, 275-310.

Timoshenko, J., Duan, Z., Henkelman, G., Crooks, R. M. & Frenkel, A. I. (2019). *Annu. Rev. Anal. Chem.* **12**, 501–522.

Timoshenko, J., & Frenkel, A. I. (2017). *Catal. Today* **280**, 274-282.

Timoshenko, J. & Frenkel, A. I. (2019), *ACS Catal*. **9**, 10192-10211

Torrisi, S. B., Carbone, M. R., Rohr, B. A., Montoya, J. H., Ha, Y., Yano, J., Suram, S. K. & Hung, L. (2020). *Npj Comput. Mater*. **6**, 109.

Ueda, S. (2013). *J. Electron Spectros. Relat. Phenomena* **190**, 235-241.

Vaccari, M., Aquilanti, G., Pascarelli, S. & Mathon, O. (2009). *J. Phys. Condens. Matter*. **21**, 145403.

Vinson, J., Rehr, J. J., Kas, J. J., & Shirley, E. L. (2011). *Phys. Rev. B.* **83**, 115106.

Wang, L., Zhang, Z., & Han, X. (2013). NPG Asia Mater. **5**, e40.

Wende, H. (2004). *Reports Prog. Phys.* **67**, 2105–2181.

Yamamoto, T. (2008). *X-Ray Spectrom.* **36**, 572–584.

Yancey, D. F., Chill, S. T., Zhang, L., Frenkel, A. I., Henkelman, G. & Crooks, R. M. (2013). *Chem. Sci.* **4**, 2912–2921.

Yevick, A. & Frenkel, A. I. (2010). *Phys. Rev. B – Condens. Matter. Mater. Phys*. **81**, 115451.

Supplementary Information

Table S1 Fabrication parameters for TiGDC20 samples

	Sputtering process	Pressure	Gas Flow	Power	Deposition Time
#1	Co-sputtered from Ti and 20 mol% Gd in CeO2 stoichiometric target.	20 mTorr	30 SCCM Ar	100 Watt GDC 150 Watt Ti	4h
#2	Reactive co-sputtered from Ti and 20 mol% Gd in Ce alloy target.	15 mTorr	35 SCCM Ar	110 Watt GDC 150 Watt Ti	3h

Table S2 Fabrication parameters for the VGDC20 sample

Sputtering process	Pressure	Gas Flow	Power	Deposition Time
Co-sputtered from V and 20 mol% Gd in CeO2 stoichiometric target.	20 mTorr	30 SCCM Ar	100 Watt GDC	VGDC20

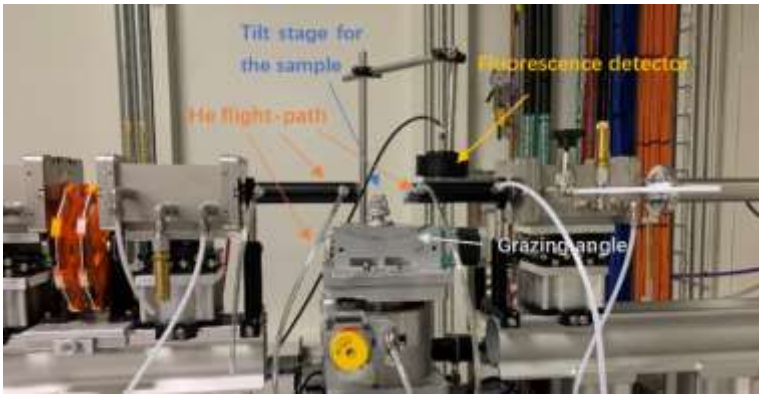

Figure S1 Ex-situ experimental setup at the QAS beamline. The data were collected at grazing incidence. The grazing angle is 2 degrees. The blue arrow shows the sample stage. The fluorescence detector was positioned at the top of the sample stage (indicated by the yellow arrow). Helium gas was flown in a flight tube/path to reduce the X-ray absorption by air.

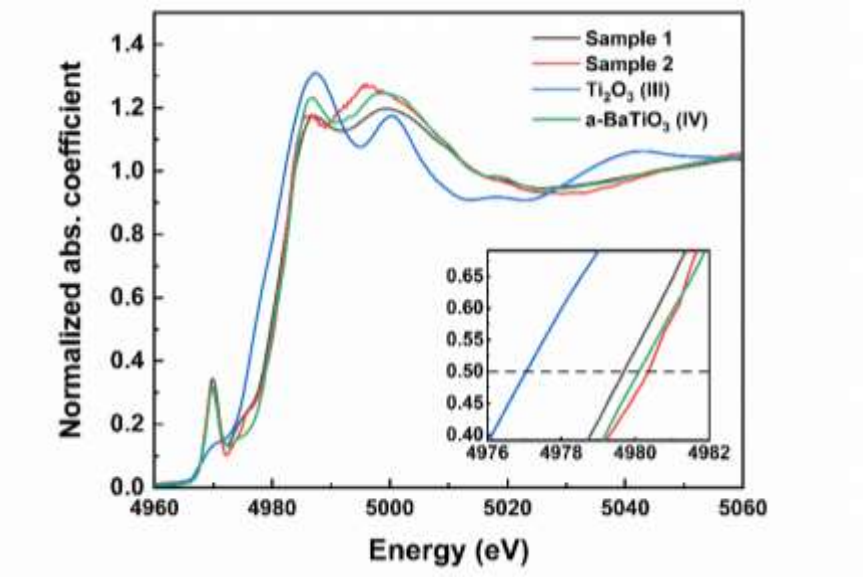

Figure S2 Ti K-edge XANES spectra of sample 1, sample 2, Ti_2O_3, and amorphous $BaTiO_3$. The inset shows the region near the 0.5 edge step (McKeown, 2002) used to qualitatively estimated the changes in the charge state between the samples and reference compounds, with states (III) and (IV).

S1. Pre-edge fitting processes

The pre-edge peak fitting processes were performed by Athena software. The error function was used to model the main edge step. Pseudo-Voigt and Gaussian functions were used to model the main pre-edge peak and the high energy pre-edge feature, respectively.

References

McKeown, D. A., Muller, I. S., Matlack, K. S., & Pegg, I. L. (2002). *J. Non-Cryst. Solids*, **298**, 160-175.